

Article

Metallogenesis of the Bawang Sn-Zn Polymetallic Deposit, Wuxu Ore Field, Guangxi, South China: U-Pb Dating and C-O-S-Pb Isotopic Constraints

Enyun Liang ^{1,2,3,*}, Dezhi Huang ^{1,2}, Guangqian Zeng ^{3,4}, Gengyin Liu ³, Guangjun Zou ^{3,5}, Peng Luo ³ and Di Chen ³

¹ Key Laboratory of Metallogenetic Prediction of Nonferrous Metals and Geological Environment Monitoring Ministry of Education, School of Geoscience and Infophysics, Central South University, Changsha 410083, China; dzhuang_01@163.com

² Hunan Key Laboratory of Nonferrous Resources and Geological Hazards Exploration, Changsha 410083, China

³ Hunan Institute of Geological Survey, Changsha 410116, China; zengguangqian90@163.com (G.Z.); liugengyin321@163.com (G.L.); zouguangjun182@163.com (G.Z.); lxc_hngs@163.com (P.L.); cd20210611@163.com (D.C.)

⁴ Institute of Geomechanics, Chinese Academy of Geological Sciences, Beijing 100081, China

⁵ College of Earth Sciences, Chengdu University of Technology, Chengdu 610059, China

* Correspondence: 8832188@163.com



Citation: Liang, E.; Huang, D.; Zeng, G.; Liu, G.; Zou, G.; Luo, P.; Chen, D. Metallogenesis of the Bawang Sn-Zn Polymetallic Deposit, Wuxu Ore Field, Guangxi, South China: U-Pb Dating and C-O-S-Pb Isotopic Constraints. *Minerals* **2022**, *12*, 137. <https://doi.org/10.3390/min12020137>

Academic Editor: Maria Boni

Received: 13 January 2022

Accepted: 21 January 2022

Published: 25 January 2022

Publisher's Note: MDPI stays neutral with regard to jurisdictional claims in published maps and institutional affiliations.



Copyright: © 2022 by the authors. Licensee MDPI, Basel, Switzerland. This article is an open access article distributed under the terms and conditions of the Creative Commons Attribution (CC BY) license (<https://creativecommons.org/licenses/by/> 4.0/).

Abstract: The Bawang deposit, located in the west of Wuxu ore field, southern section of the Nandan-Hechi metallogenic belt, is a medium-sized tin-zinc polymetallic deposit. Its genesis has been a matter of debate because of lacking constraints from isotope geology. In this study, LA-MC-ICP-MS U-Pb dating of cassiterite and C-O-S-Pb isotope analyses of monominerals were used to investigate the mineralization age and source of the ore-forming minerals in the Bawang deposit. LA-ICP-MS U-Pb dating of cassiterite yielded ages of 93.1 ± 4.8 Ma and 85.3 ± 6.3 Ma, indicating that the mineralization occurred in the early Late Cretaceous. The $\delta^{13}\text{CPDB}$ and $\delta^{18}\text{OSMOW}$ values of calcites at the ore stage range between -0.41‰ and 0.44‰ (average = -11‰) and between 13.8‰ and 15.40‰ (average = 14.59‰), respectively. This shows that ore fluid sources were a mixture of those derived from magma and stratum. Pyrite and sphalerite have uniform $\delta^{34}\text{S}$ values ($-4.45\text{‰} \sim -2.20\text{‰}$), indicating that sulfur is also derived from the mixing of magmatic hydrothermal and stratum fluids. The Pb isotopic composition of sulfide ($^{206}\text{Pb}/^{204}\text{Pb} = 18.4055 \sim 18.7625$, $^{207}\text{Pb}/^{204}\text{Pb} = 15.6745 \sim 15.7209$, $^{208}\text{Pb}/^{204}\text{Pb} = 38.6232 \sim 39.0370$) is consistent with the granite of the same age, indicating that ore-forming metals are mainly derived from magmatic hydrothermal solution. The Bawang deposit is a hydrothermal vein-type deposit in the external contact zone of Late Cretaceous granite, controlled by tectonic fractures, and formed by the interaction of magmatic hydrothermal fluid and carbonate rock. There may be large skarn-type ore bodies in the deep part. The results of this study provide insights into the research and exploration of similar deposits in Nandan-Hechi metallogenic belt and in the Youjiang Basin.

Keywords: cassiterite; LA-MC-ICP-MS U-Pb dating; C-O-S-Pb isotope; Bawang tin-zinc polymetallic deposit; Nandan-Hechi metallogenic belt; Youjiang Basin

1. Introduction

Chronological information on mineralization is key to understanding the genesis of ore deposits. In recent years, LA-ICP-MS U-Pb dating of cassiterite has been used to study the metallogenetic age of tin polymetallic deposits [1–6]. Furthermore, C-O-S-Pb isotope analysis has been shown to be an effective method for determining the source of ore fluids and metals [7–11]. In this paper, U-Pb isotope chronology was carried out on the Bawang

deposit to obtain accurate age data. Supplemented by the study of C-O-S-Pb isotopes, evidence for the sources of mineralized fluids and substances is explored.

The Danchi mineralization belt, located in the Nandan-Hechi area of northwest Guangxi, is a NW-trending tin polymetallic mineralization belt about 100 km long and 30 km wide, with four ore fields distributed along strike [12]. There are more than 200 mineral deposits and occurrences of tin, tungsten, molybdenum, copper, lead, zinc, silver, and mercury, including two super-large deposits and 13 large-medium deposits [13,14]. For more than half a century, geologists have carried out systematic studies on the petrology, mineralogy, geochemistry, and chronology in this belt [13–40]. Nevertheless, there are still great controversies regarding the origin of the deposits, mainly forming three different understandings: (i) submarine exhalation–sedimentation [15,16]; (ii) postmagmatic hydrothermal [17–21]; and (iii) exhalation sedimentation and magmatic hydrothermal superposition [22–24]. Most of the previous studies focused on stratiform ore bodies, and the age analysis of ore deposits was mainly concentrated in Dachang ore field. Bawang deposit, located in the west of Wuxu ore field, is a medium-sized tin–zinc polymetallic deposit. Unlike other stratiform deposits in the area, the stratiform ore bodies are connected with those cutting strata, controlled by the shear faults, which provides an opportunity for studying the genesis of tin polymetallic mineralization from another perspective.

2. Regional Geology

The Nandan-Hechi metallogenic belt is located to the southeast of the Yangtze Plate (Figure 1a), southwest of the Ghiangnania, and on the northeast side of the Youjiang Basin. It is a composite part of the Paleo-Tethys tectonic domain and the Pacific tectonic domain [38]. The range of the metallogenic belt is similar to that of the Nandan-Hechi Hercynian-Indosinian faulted fold belt (Figure 1b). After the Caledonian movement, the area was continuously depressed in the Paleozoic and Early Mesozoic and strongly folded in the Indosinian and Yanshanian. Along with strong intermediate-acid magmatic activity, a large number of tin polymetallic minerals were produced [39].

The Wuxu ore field is located in the south of the Nandan-Hechi mineralization belt. The formations from the Lower Devonian to Middle Triassic are exposed, dominated by Middle and Upper Devonian (Figure 1c). The lithology of Middle Devonian to Middle Permian is carbonate with clasolite and silicolite. The Lower Devonian/Upper Permian to Middle Triassic is dominated by clasolite interspersed with carbonate. The Tangding Formation ($D_{1-2}t$), comprising mudstone, argillaceous siltstone, and sandy mudstone, is the main host rock of Pb-Zn-Sn-Sb deposits. The Nandan Formation (C_2P_1n), comprising calcarenite, is a secondary ore-bearing horizon. The marl and bioclastic limestone of the Luofu Formation (D_2l), the siliceous shale of the Liujiang Formation (D_3l), and the banded limestone of the Wuzhishan Formation (D_3w) are host rocks of arsenic–mercury deposits [13]. The Wuxu Anticline, Bayue Syncline, and Jiuxu Anticline are the main fold structures and are all NNW-trending (Figure 1d), belonging to the southern extension of the NW-trending Danchi Anticline. It is believed that deflection of the fold axial trace was the result of superimposition of the late SN-trending fold [17]. There are NNW-, NNE-, NE-, and nearly EW-trending faults, with predominant faults trending NNW and NNE, distributed in the core of the Wuxu Anticline, arranged in parallel groups dipping steeply (dip angle of >60 degrees). These faults and fractures are the main ore-controlling structures, and the Shuiluo, Jianzhupo, Furongchang, and Bawang deposits are controlled by this group of structures [14]. There is no migmatite exposed, but it is speculated that concealed granite lies 3~10 km to the north of Jianzhupo deposit [40].

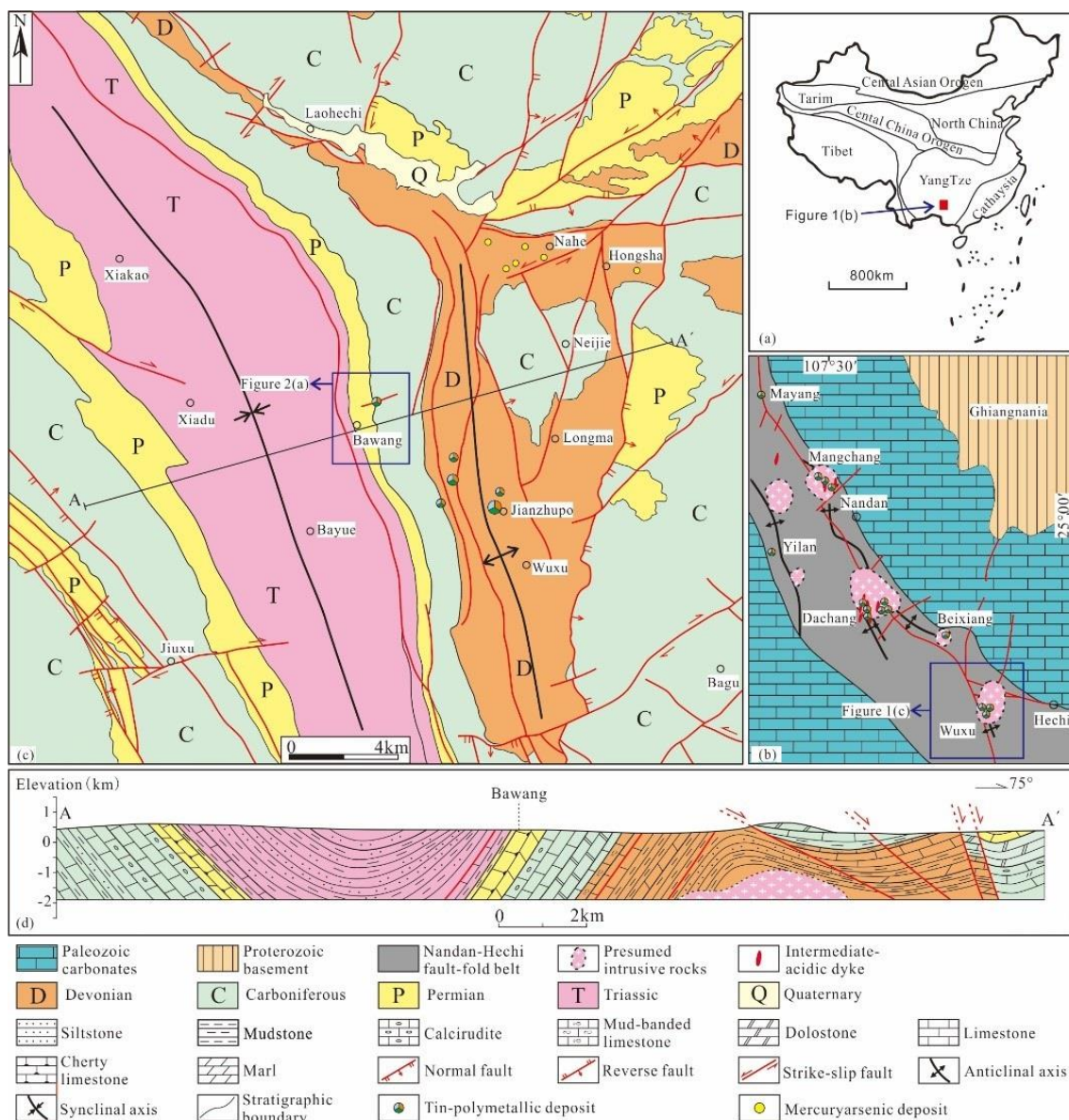


Figure 1. Geotectonic location map of the Bawang deposit (a); sketch map showing structural geology and mineral distribution of the Nandan-Hechi metallogenic belt (b); geological and deposit distribution map of the Wuxu ore field (c); structural sections of Wuxu ore field (d).

3. Ore Deposit Geology

The Bawang deposit is located in the west of the Wuxu ore field and the west wing of the Wuxu Anticline. The strata exposed include Upper Carboniferous Baping, Dashantang, Upper Carboniferous/Lower Permian Nandan, Middle Carboniferous Sidazhai, Upper Carboniferous Linghao, Lower Triassic Shipao, and Middle Triassic Baifeng formations, and a Quaternary system (Figure 2a). The Baping Formation is composed of thin microcrystalline limestone, argillaceous limestone interlaced with chert limestone, silicilite, mudstone, and siltstone. The Dashantang Formation is thick dolomite with dolomitic limestone. The Nandan Formation is divided into four sections: the first section is chert belt limestone and fine crystal limestone mixed with dolomitic limestone; the second section is aplite and silty limestone; the third section is interbedded with thin–medium siltstone limestone and dolomitic limestone, containing a small amount of chert belts and nodules; and the fourth section is thick calcirudite intercalated with calcisiltite. The Sidazhai Formation is composed of two sections: the lower section is medium-thickness calcarenite and calcisiltite

containing chert, sandwiched with bioclastic calcarenite, and the upper section is medium calcisiltite with chert belts and nodules. The third and fourth sections of the Nandan Formation are host rock of the ore deposit.

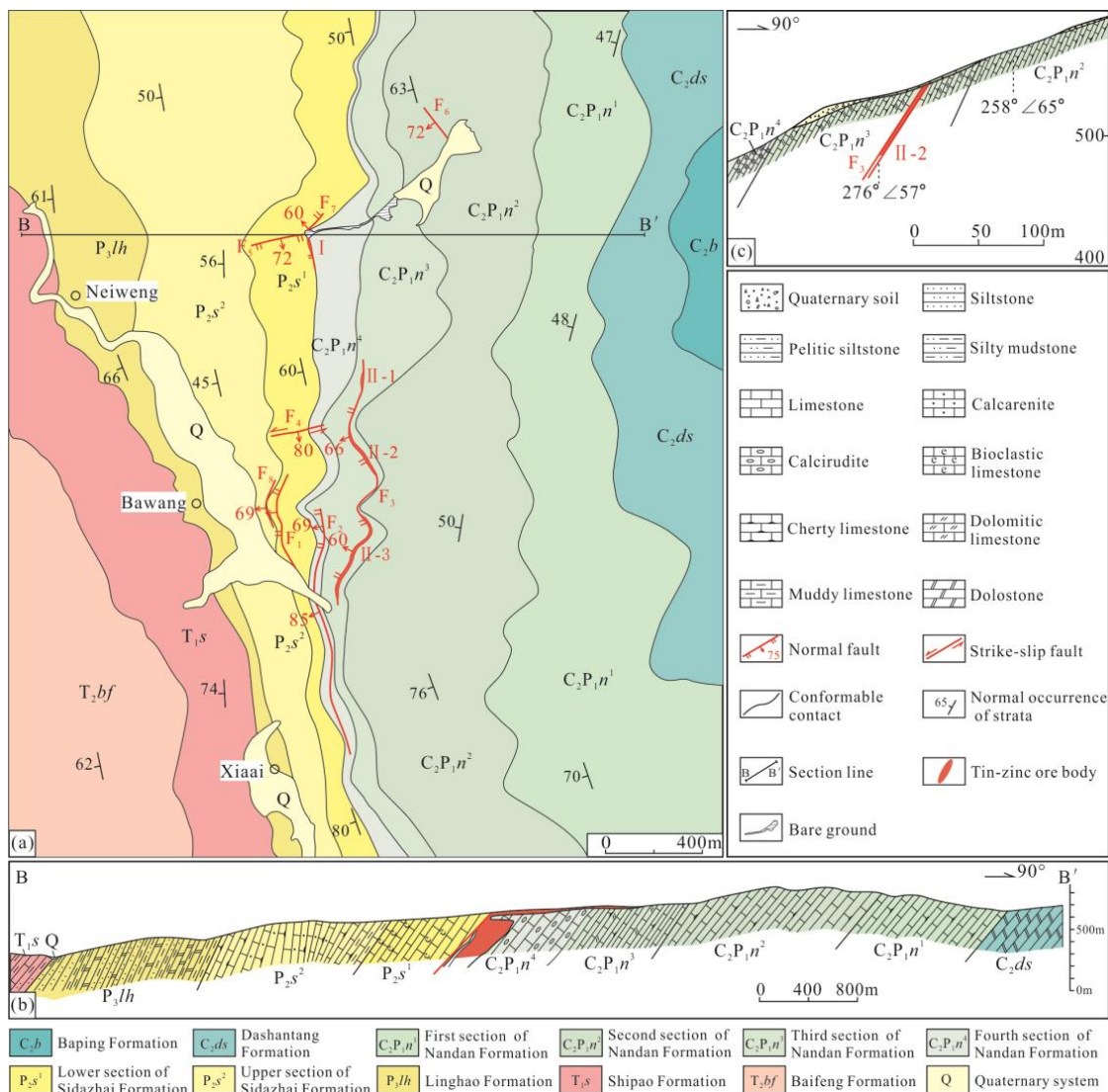


Figure 2. Geological sketch map (a) and ore-controlling structural styles (b,c) of the Bawang deposit.

The strata in the Bawang deposit are monocline (Figure 2b). The strike of the strata is nearly SN and NNW, the dip direction ranges from 240° to 290°, and the dip angle is mostly 35°~60°. The fault structure is generally developed, trending N-S, E-W, and NW-SE. The F₃ fault is located in the middle of the mining area, in which three tin-zinc ore bodies (II-1, II-2, II-3) occur (Figure 2c). It is a S-N trending tensional normal fault with a length of about 1 km, dip direction of 260°~280°, and dip angle of 55°~66°. The F₅ fault is located in the north-central mining area, hosting I ore body. This fault is a zone formed by a series of overlapping dense fractures (joints) striking NEE-NE, with SSE-SE dipping at high angles and reversing locally. The fault is sinistral strike-slip thrusting in the early stage, becoming left-normal-slip in the late stage.

The I ore body is the main one, extending down to 730 m (Figure 3a), 0.33~25.95 m thick, with an average thickness of 9.19 m. The major metal is zinc, associated with Sn, Ag, In, Cd, Ga, and As. The average grade of Zn is 7.09%, Sn 0.70%, Ag 46.79 g/t, In 0.0361%, Cd 0.073%, Ga 0.0061%, and As 1.34%. The I ore body is strictly controlled by the F₅ fault, formed similar to a tube with west side-pitching. In fact, it is an ore body group

composed of several bonanzas divided by non-ore surrounding rock (the fourth section of the Nandan Formation, gravel limestone). Most of the single bonanzas dip steeply to the south, and their attitudes are 172° – $182^\circ \angle 76^\circ$ – 86° , while some bonanzas are nearly upright or reverse to the north. The plane shape of the bonanza in each level resembles a dumbbell or lotus root, while some are irregular sacs (Figure 3b,c), with a plane length of 40–88 m. The shallow part of the ore body is oxidized (Figure 4a–c) while the deep part is sulfide (Figure 4d,e); their boundary is at about the 500 m level. Primary sulfides are mostly massive, but rarely have disseminated and breccia structures. The metal minerals include sphalerite, pyrite, arsenopyrite, cassiterite, pyrrhotite, chalcopyrite, and so on (Figure 4f–l). The gangue minerals are calcite and dolomite. The wallrock alteration is weak, including limonitization, carbonation, pyritization, and silicification, with a clear boundary to the ore body.

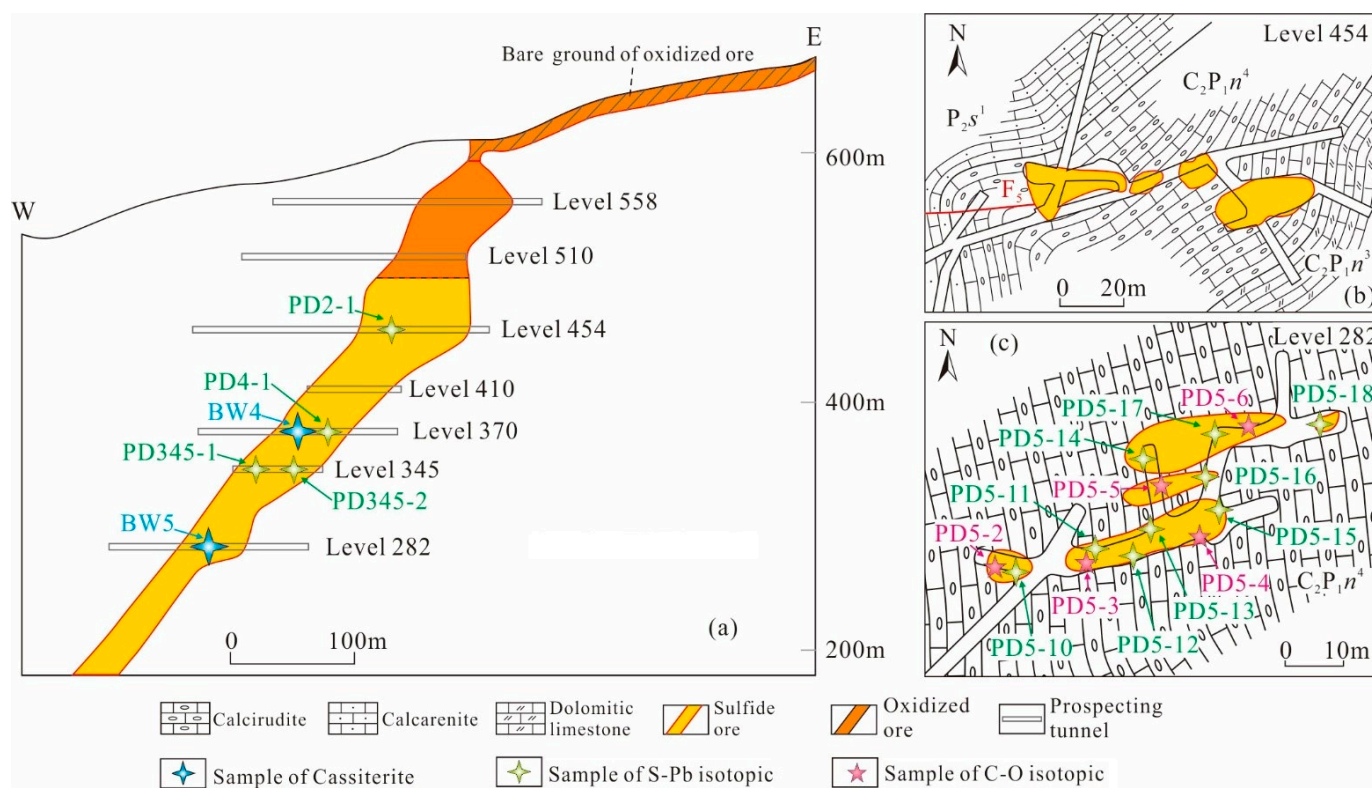


Figure 3. Vertical projection showing the regularity of side-pitching of the I ore body in Bawang deposit (a); geological plan of level 454 (b) and 282 (c).

The II ore body is hosted in bed sliding fracture zone F₃ and is oxidized. It consists of II-1, II-2, and II-3. Their attitudes are 245° – $277^\circ \angle 55^\circ$ – 66° ; their lengths are 50, 240, and 360 m, respectively; and their thicknesses are 1.00–1.91 m. Ore contains 0.26%–1.44% Pb, 0.79%–10.92% Zn, and 0.01%–0.56% Sn. The metal minerals are limonite, sphalerite, cassiterite, galena, and so on, while the gangue minerals are mainly calcite.

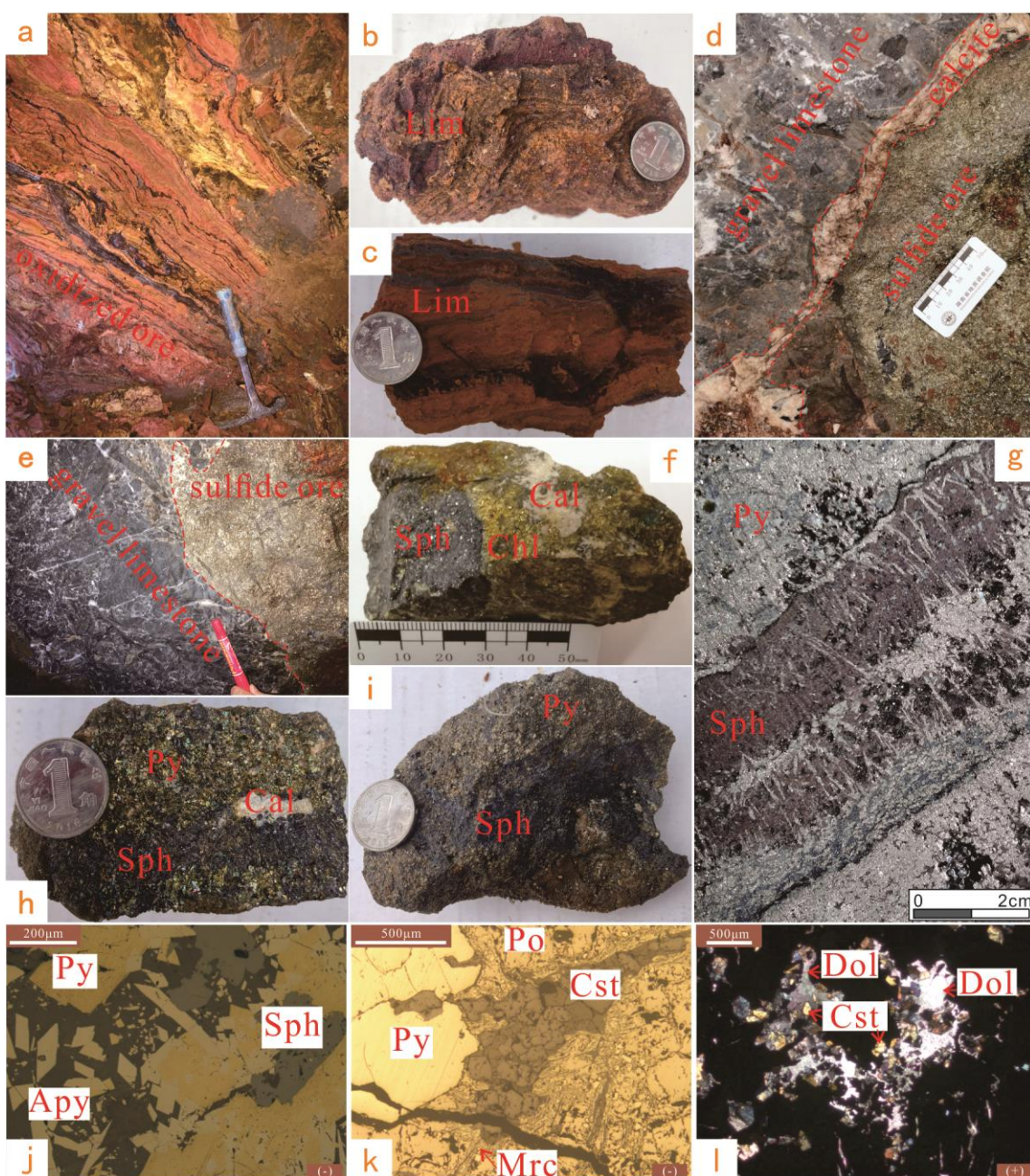


Figure 4. Typical photos of the Bawang deposit: (a–c) the oxidized ore; (d,e) the sulfide ore has a clear boundary; (f–i) metal minerals; (j) pyrite and arsenopyrite associated with sphalerite; (k) pyrite, pyrrhotite, and marcasite associated with cassiterite; (l) the edge of the dolomite dotted with cassiterite. Abbreviations: Lim = limonite, Cal = calcite, Sph = sphalerite, Chl = chalcopyrite, Py = pyrite, Apy = arsenopyrite, Po = pyrrhotite, Cst = cassiterite, Mrc = marcasite, Dol = dolomite.

4. Sample Collection and Analytical Methods

4.1. Cassiterite U-Pb Isotope Dating

The two samples BW4 and BW5 collected for cassiterite U-Pb isotope dating were, respectively, obtained from levels 370 and 282 of the I ore body (Figure 3a). Heavy minerals were separated by gravity concentration, and cassiterite grains were hand-picked under a binocular microscope. Large grains with better transparency and fewer cracks and inclusions were selected as targets. Images were taken under transmitted light, reflected light, and backscattered electron (BSE). In the BSE images, most cassiterites were semi-idiomorphic

and tetragonal, but a few were irregular. There was almost no aberration in the BSE images, indicating that the composition was relatively uniform (Figure 5).

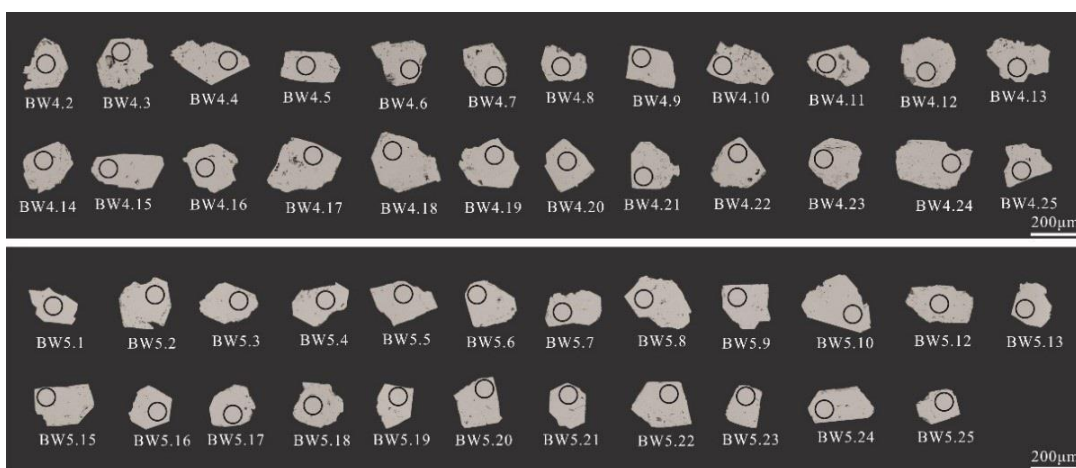


Figure 5. The backscattered electron (BSE) images of cassiterites from the Bawang deposit.

The U-Pb isotopic dating of cassiterite was completed in the Isotope Geochemistry Laboratory at the Tianjin Center of China Geological Survey [41]. The instrument was composed of a Thermo Fisher Neptune multireceiver inductively coupled plasma mass spectrometer and an ESI UP193-FX ArF excimer laser ablation sampling system. The experimental process was as follows: According to the reflected light and backscattered electron images of cassiterite, the areas with few inclusions and cracks were tested. Cassiterite grains were analyzed using an energy density of 15 J/cm^2 , a spot size of $75 \mu\text{m}$, and a repetition rate of 20 Hz. Helium gas carrying the ablated sample aerosol was mixed with argon and nitrogen (additional diatomic gas) to enhance sensitivity and was finally flowed into the ICP-MS instrument. Due to the weak ion signal of ^{204}Pb and the interference of ^{204}Hg in argon gas, the content of ^{204}Pb is difficult to accurately determine. Therefore, ^{207}Pb can be used instead of ^{204}Pb as the U-Pb isochron for young cassiterite samples (generally less than 400 Ma) with low U content and low ^{207}Pb content. That is, the $^{206}\text{Pb}/^{207}\text{Pb}$ - $^{238}\text{U}/^{207}\text{Pb}$ isochron replaces the traditional $^{238}\text{U}/^{204}\text{Pb}$ - $^{206}\text{Pb}/^{204}\text{Pb}$ isochron method for data processing [42]. A standard sample (AY-4, $^{206}\text{Pb}/^{238}\text{U}$ age = 158.2 ± 0.4 Ma) with accurately determined ID-TIMS U-Pb age was used as the external standard [43]. Data calculation and graph drawing of the $^{206}\text{Pb}/^{207}\text{Pb}$ - $^{238}\text{U}/^{207}\text{Pb}$ isochron and $^{207}\text{Pb}/^{206}\text{Pb}$ - $^{238}\text{U}/^{206}\text{Pb}$ concordance ages (Tera-Wasserburg curve) were performed using Isoplot software [44,45].

4.2. C-O-S-Pb Isotopes

The samples used for C-O isotope analysis were ore-stage calcite collected from level 282. S-Pb isotope samples were sphalerite and pyrite from the mineralization period; PD2-1 was from level 454, PD4-1 was from level 370, PD345-1 and PD345-2 were from level 345, and others were from level 282. Firstly, the samples were crushed and sieved, taking the particles between 40 and 60 mesh. Then, repeated selection was carried out until the purity of the single mineral was greater than 99%. At last, the samples were ground to less than 200 mesh in an agate mortar. C-O-S-Pb isotope tests were completed by Langfang Chengxin Geological Services Co., LTD (Langfang, China).

The calcite samples were ground to 200 mesh and baked in an oven at 105°C for 2 h to remove adsorbed water. The sample tubes were baked for 30 min in a Gasbench at 70°C . Then, about 0.2 mg of carbonate was placed into the sample tubes and capped. The air in the sample tube was evacuated by high-purity helium gas. The prepared calcite powder and pure (100%) phosphoric acid were fully reacted for more than 8 h, producing CO_2 gas. The CO_2 gas was carried into a MAT253 mass spectrometer with high-purity helium to analyze the C and O isotope composition. Every five samples were added into a group

of standard GBW04416 and GBW04417 to compare. Analytical results are reported in δ notation as per mil (‰) deviation relative to the Vienna Pee Dee Belemnite (VPDB) as $\delta^{13}\text{C}_{\text{V-PDB}}$ and $\delta^{18}\text{O}_{\text{V-PDB}}$, and the $\delta^{18}\text{O}_{\text{V-SMOW}}$ value was calculated using the equation of Friedman and O’Neil [46], i.e., $\delta^{18}\text{O}_{\text{V-SMOW}} = 1.03086 \times \delta^{18}\text{O}_{\text{V-PDB}} + 30.86$. The analytical accuracy was better than $\pm 0.1\text{‰}$ (2σ) for both C and O isotopes.

Sulfide monominerals and cuprous oxide were ground to about 200 mesh and mixed evenly in a certain proportion. Then, they were heated to 980 °C in a vacuum of 2.0×10^{-2} Pa, with the oxidation reaction generating sulfur dioxide gas. The sulfur dioxide gas was collected by a freezing method under vacuum conditions, and the sulfur isotopic composition was analyzed by Delta V Plus gas isotope mass spectrometry. The measured results were based on CDT, recorded as $\delta^{34}\text{S}_{\text{V-CDT}}$. The analytical accuracy was better than $\pm 0.2\text{‰}$.

A 0.1–0.2 g powder sample was accurately weighed and dissolved in a low-pressure airtight dissolution tank with mixed acid (HF + HNO₃ + HClO₄) for 24 h. After the sample was completely dissolved, it was converted into chloride by adding 6 mol/L hydrochloric acid and then dried. The solution was dissolved with 1 mL of 0.5 mol/L HBr and centrifugation. The liquid was added to an anion exchange column (250 μL AG1-X8, 100–200 mesh). The impurities were washed with 0.5 mol/L HBr, and the lead was resolved with 1 mL of 6 mol/L HCl in a PTFE beaker. An ISOPROBE-T thermal ionization mass spectrometer was used for isotope analysis. The samples were placed on a rhenium band with silica gel phosphate and the lead isotope ratio was measured by the static acceptance method. NBS 981 uncorrected results: $^{208}\text{Pb}/^{206}\text{Pb} = 2.164940 \pm 15$, $^{207}\text{Pb}/^{206}\text{Pb} = 0.914338 \pm 7$, $^{204}\text{Pb}/^{206}\text{Pb} = 0.0591107 \pm 2$; Pb background was less than 100 pg during the whole process.

5. Results

5.1. Cassiterite U-Pb Isotope Dating

The results of LA-ICP-MS U-Pb dating of the cassiterite are shown in Table 1 and Figure 6. Sample BW4 had 24 measuring points, and the ratios of $^{238}\text{U}/^{206}\text{Pb}$, $^{238}\text{U}/^{207}\text{Pb}$, and $^{206}\text{Pb}/^{207}\text{Pb}$ ranged from 3.11 to 28.29, from 3.55 to 53.36, and from 1.2386 to 1.9695, respectively. The $^{207}\text{Pb}/^{206}\text{Pb}$ - $^{238}\text{U}/^{206}\text{Pb}$ concordant age was 93.1 ± 4.8 Ma ($n = 24$, MSWD = 1.5) (Figure 6a), the $^{206}\text{Pb}/^{207}\text{Pb}$ - $^{238}\text{U}/^{207}\text{Pb}$ isochron age was 89.3 ± 6.3 Ma ($n = 24$, MSWD = 0.86), and the initial $^{206}\text{Pb}/^{207}\text{Pb}$ ratio was 1.183 ± 0.02 (Figure 6b). Sample BW5 had 25 measuring points, and the ratios of $^{238}\text{U}/^{206}\text{Pb}$, $^{238}\text{U}/^{207}\text{Pb}$, and $^{206}\text{Pb}/^{207}\text{Pb}$ ranged from 3.19 to 34.49, from 2.78 to 69.68, and from 1.2519 to 2.1045, respectively. The $^{207}\text{Pb}/^{206}\text{Pb}$ - $^{238}\text{U}/^{206}\text{Pb}$ concordant age was 85.3 ± 6.3 Ma ($n = 23$, MSWD = 2.1) (Figure 6c), the $^{206}\text{Pb}/^{207}\text{Pb}$ - $^{238}\text{U}/^{207}\text{Pb}$ isochron age was 82.9 ± 5.3 Ma ($n = 23$, MSWD = 1.08), and the initial $^{206}\text{Pb}/^{207}\text{Pb}$ ratio was 1.218 ± 0.014 (Figure 6d). The two samples’ concordant ages and isochron ages are consistent within the error range, indicating that the metallogenetic ages obtained in this study are reliable.

Table 1. LA-ICP-MS U-Pb dating of cassiterite in the Bawang deposit.

Fraction	U-Pb Isochron Age/Ma				U-Pb Concordant Age (Tera-Wasserburg)/Ma			
	$^{238}\text{U}/^{206}\text{Pb}$	2σ	$^{207}\text{Pb}/^{206}\text{Pb}$	2σ	$^{238}\text{U}/^{207}\text{Pb}$	2σ	$^{206}\text{Pb}/^{207}\text{Pb}$	2σ
BW4.2	9.20	4.89	0.7697	3.42	11.21	4.81	1.2993	3.42
BW4.3	17.31	3.21	0.6649	4.06	24.57	3.39	1.5039	4.06
BW4.4	19.27	4.20	0.6199	5.58	29.51	4.97	1.6133	5.58
BW4.5	25.36	4.90	0.5436	5.15	43.37	6.66	1.8395	5.15
BW4.6	23.85	3.83	0.5761	5.47	39.74	4.13	1.7357	5.47
BW4.7	21.62	4.54	0.6054	7.58	35.10	5.42	1.6519	7.58
BW4.8	19.73	3.55	0.6048	5.44	31.27	3.76	1.6534	5.44
BW4.9	16.39	2.32	0.6590	3.16	23.30	2.12	1.5174	3.16
BW4.10	17.04	3.64	0.6643	4.71	24.44	3.34	1.5054	4.71

Table 1. Cont.

Fraction	U-Pb Isochron Age/Ma				U-Pb Concordant Age (Tera-Wasserburg)/Ma			
	$^{238}\text{U}/^{206}\text{Pb}$	2σ	$^{207}\text{Pb}/^{206}\text{Pb}$	2σ	$^{238}\text{U}/^{207}\text{Pb}$	2σ	$^{206}\text{Pb}/^{207}\text{Pb}$	2σ
BW4.11	25.52	4.40	0.5937	6.55	42.03	4.59	1.6845	6.55
BW4.12	22.48	4.01	0.6146	5.61	35.15	4.30	1.6270	5.61
BW4.13	14.79	3.20	0.7018	4.60	20.02	3.25	1.4250	4.60
BW4.14	13.30	3.44	0.6847	4.85	18.42	4.08	1.4605	4.85
BW4.15	6.32	14.50	0.7651	5.06	7.60	15.82	1.3070	5.06
BW4.16	3.11	5.89	0.8074	1.76	3.55	6.01	1.2386	1.76
BW4.17	25.40	4.63	0.5325	8.88	46.72	7.45	1.8779	8.88
BW4.18	24.92	7.55	0.5311	5.60	41.80	10.34	1.8830	5.60
BW4.19	17.08	2.49	0.6559	3.53	24.40	2.68	1.5247	3.53
BW4.20	6.21	31.75	0.7312	5.85	7.49	33.64	1.3677	5.85
BW4.21	28.29	5.44	0.5077	7.81	53.36	7.63	1.9695	7.81
BW4.22	21.80	3.20	0.6038	4.54	34.24	3.38	1.6561	4.54
BW4.23	13.16	5.83	0.6999	4.09	17.54	6.54	1.4288	4.09
BW4.24	8.36	3.57	0.7563	3.39	10.32	3.83	1.3222	3.39
BW4.25	19.29	4.51	0.6365	4.30	28.16	5.78	1.5710	4.30
BW5.1	20.93	3.86	0.6006	5.78	33.47	4.36	1.6650	5.78
BW5.2	15.43	5.61	0.6608	3.97	21.78	6.36	1.5132	3.97
BW5.3	11.36	7.94	0.6952	4.72	15.20	9.29	1.4385	4.72
BW5.4	12.54	3.36	0.7011	3.51	16.82	3.24	1.4263	3.51
BW5.5	18.49	2.83	0.6173	2.93	27.84	3.33	1.6201	2.93
BW5.6	23.91	4.45	0.5792	5.04	38.27	6.42	1.7266	5.04
BW5.7	16.74	3.28	0.6464	4.12	24.52	3.10	1.5469	4.12
BW5.8	23.97	3.73	0.5775	5.60	39.58	4.69	1.7315	5.60
BW5.9	18.19	5.98	0.6356	8.08	26.92	6.88	1.5733	8.08
BW5.10	24.07	4.87	0.5962	6.92	39.71	5.04	1.6773	6.92
BW5.12	6.64	2.77	0.7399	3.13	8.40	2.75	1.3515	3.13
BW5.13	3.19	26.59	0.7738	2.78	3.65	27.63	1.2923	2.78
BW5.15	12.94	3.48	0.7352	4.36	16.62	3.86	1.3601	4.36
BW5.16	2.43	10.86	0.7988	1.09	2.78	11.26	1.2519	1.09
BW5.17	22.79	3.83	0.5828	4.70	36.67	5.03	1.7160	4.70
BW5.18	16.94	2.85	0.6559	3.46	24.21	2.93	1.5246	3.46
BW5.19	11.91	5.58	0.7190	4.79	15.65	6.00	1.3909	4.79
BW5.20	21.62	4.22	0.5900	4.96	34.77	4.64	1.6949	4.96
BW5.21	17.41	3.34	0.6705	4.42	24.50	3.78	1.4915	4.42
BW5.22	34.49	4.02	0.4752	6.30	69.68	5.20	2.1045	6.30
BW5.23	20.37	4.14	0.6436	5.80	30.55	4.53	1.5537	5.80
BW5.24	9.02	6.43	0.7600	3.92	11.08	6.92	1.3157	3.92
BW5.25	13.47	6.37	0.6743	3.60	18.97	4.21	1.4829	3.60

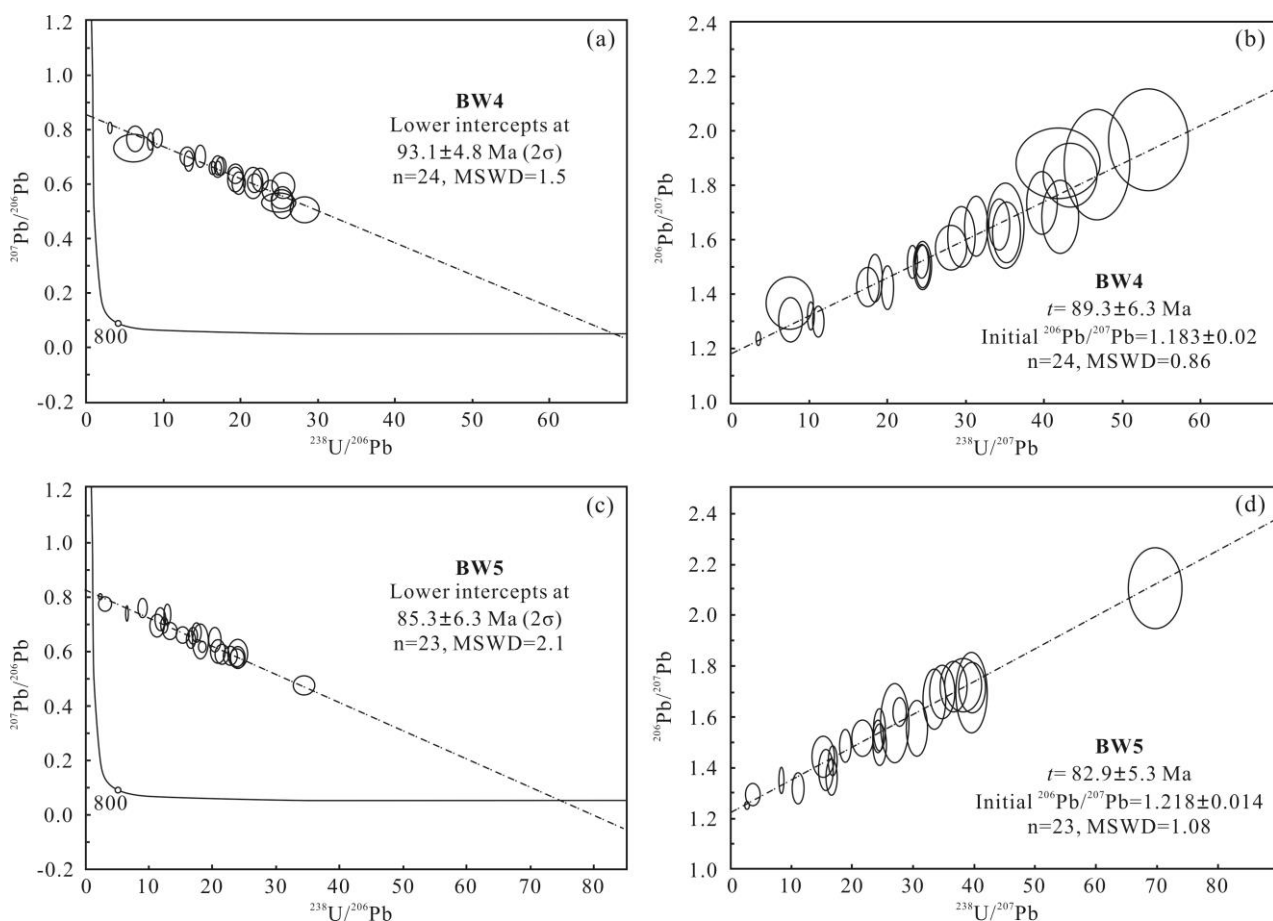


Figure 6. U–Pb concordia diagrams (Tera–Wasserburg) and isochron diagrams of cassiterites from the Bawang deposit. (a): concordant age of BW4, (b): isochron age of BW4, (c): concordant age of BW5, (d): isochron age of BW5.

5.2. C–O Isotopes

Carbon–oxygen isotope results for the five calcite samples (during the mineralization period) from the Bawang deposit are given in Table 2. The $\delta^{13}\text{C}_{\text{PDB}}$ values are not significantly different, ranging from $-0.41\text{\textperthousand}$ to $0.44\text{\textperthousand}$, with a range of $0.85\text{\textperthousand}$ and an average of $-0.11\text{\textperthousand}$. The $\delta^{18}\text{O}_{\text{V-PDB}}\text{\textperthousand}$ ranged from $-16.50\text{\textperthousand}$ to $-15.00\text{\textperthousand}$, with a range of $1.5\text{\textperthousand}$ and an average of $-15.09\text{\textperthousand}$. $\delta^{18}\text{O}_{\text{V-SMOW}}\text{\textperthousand}$ ranged from $13.85\text{\textperthousand}$ to $15.40\text{\textperthousand}$, with a range of $1.55\text{\textperthousand}$ and an average of $14.59\text{\textperthousand}$.

Table 2. Carbon and oxygen isotopes compositions of ore-forming calcite from the Bawang deposit (‰).

Sample No.	$\delta^{13}\text{C}_{\text{V-PDB}}\text{\textperthousand}$	$\delta^{18}\text{O}_{\text{V-PDB}}\text{\textperthousand}$	$\delta^{18}\text{O}_{\text{V-SMOW}}\text{\textperthousand}$
PD5-2	0.44	-16.50	13.85
PD5-3	0.25	-15.80	14.57
PD5-4	-0.07	-15.21	15.18
PD5-5	0.34	-16.41	13.94
PD5-6	-0.41	-15.00	15.40

5.3. S–Pb Isotopes

Sulfur isotope compositions in the Bawang deposit are given in Table 3. The $\delta^{34}\text{S}$ values of the nine pyrite samples ranged from $-4.45\text{\textperthousand}$ to $-2.20\text{\textperthousand}$, with a range of $2.25\text{\textperthousand}$ and an average of $-3.50\text{\textperthousand}$, higher than $-5.1\text{\textperthousand}$ [47]. The $\delta^{34}\text{S}$ values of the seven sphalerite samples were concentrated, ranging from $-4.25\text{\textperthousand}$ to $-4.01\text{\textperthousand}$, with a range of $0.24\text{\textperthousand}$ and an average of $-4.17\text{\textperthousand}$, close to $-4.03\text{\textperthousand}$ [47]. In general, the $\delta^{34}\text{S}$ values of pyrite and

sphalerite at all elevations have little difference, showing a single-peak distribution, and the peak values are in the range of $-4.5\text{‰} \sim -4\text{‰}$, close to the $\delta^{34}\text{S}$ values of mantle sulfur and magmatic sulfur ($-3\text{‰} \sim +3\text{‰}$). The $\delta^{34}\text{S}$ value of sphalerite is lower than that of pyrite, indicating that sulfur isotope balance was reached in the ore-forming fluid.

Table 3. Sulfur isotopic compositions of the Bawang deposit (‰).

Sample No.	Mineral	$\delta^{34}\text{S}_{\text{V}-\text{CDT}}\text{‰}$	Reference	Sample No.	Mineral	$\delta^{34}\text{S}_{\text{V}-\text{CDT}}\text{‰}$	Reference
PD2-1	pyrite	-3.21	This study	PD5-12-2	sphalerite	-4.25	This study
PD4-1	pyrite	-4.45	This study	PD5-13-2	sphalerite	-4.01	This study
PD5-10	pyrite	-3.81	This study	PD5-15	sphalerite	-4.15	This study
PD5-12-1	pyrite	-4.06	This study	PD5-16	sphalerite	-4.23	This study
PD5-13-1	pyrite	-3.03	This study	PD5-17	sphalerite	-4.17	This study
PD5-14	pyrite	-2.20	This study	ZK1502	pyrite	-5.2	[47]
PD5-18	pyrite	-2.87	This study	CK002	pyrite	-5	[47]
PD345-1	pyrite	-3.93	This study	BW2	sphalerite	-4.1	[47]
PD345-2	pyrite	-3.96	This study	BW3	sphalerite	-3.5	[47]
PD5-2-2	sphalerite	-4.17	This study	BW4	sphalerite	-4.5	[47]
PD5-11	sphalerite	-4.20	This study				

The lead isotope compositions in the Bawang deposit are given in Table 4. They are relatively uniform, with little difference between pyrite and sphalerite. The $^{206}\text{Pb}/^{204}\text{Pb}$ ranged from 18.4055 to 18.7625, with a range of 0.375 and an average of 18.6534. The $^{207}\text{Pb}/^{204}\text{Pb}$ ranged from 15.6745 to 15.7209, with a range of 0.0464 and an average of 15.7097. The $^{208}\text{Pb}/^{204}\text{Pb}$ ranged from 38.6232 to 39.0370, with a range of 0.4138 and an average of 38.9235. The lead μ value ranged from 9.60 to 9.67 with an average of 9.66—significantly higher than the normal lead μ value (8.686~9.238). The ω values ranged from 37.32 to 38.44 with an average of 38.19, which is also higher than normal lead ω values (35.55 ± 0.59).

Table 4. Lead isotopic compositions of the Bawang deposit.

Sample No.	Mineral	$^{206}\text{Pb}/^{204}\text{Pb}$	$^{207}\text{Pb}/^{204}\text{Pb}$	$^{208}\text{Pb}/^{204}\text{Pb}$	μ	ω	Th/U	V1	V2	$\Delta\alpha$	$\Delta\beta$	$\Delta\gamma$
PD2-1	pyrite	18.7153	15.7192	39.0327	9.67	38.38	3.84	78.87	61.99	85.62	25.51	45.83
PD4-1	pyrite	18.7198	15.7202	39.0351	9.67	38.38	3.84	78.90	62.10	85.73	25.57	45.81
PD5-10	pyrite	18.6902	15.7184	39.0049	9.67	38.40	3.84	78.81	61.87	85.48	25.53	45.83
PD5-12-1	pyrite	18.6779	15.7194	38.9939	9.67	38.44	3.85	78.97	61.90	85.55	25.64	45.98
PD5-13-1	pyrite	18.7077	15.7193	39.0277	9.67	38.41	3.84	79.00	61.96	85.65	25.54	45.96
PD5-14	pyrite	18.7151	15.7202	39.0370	9.67	38.41	3.84	79.12	62.05	85.76	25.59	46.03
PD5-18	pyrite	18.5914	15.7043	38.8682	9.65	38.26	3.84	76.98	60.87	83.95	24.84	44.54
PD345-1	pyrite	18.7150	15.7161	38.9047	9.66	37.84	3.79	75.56	63.17	85.37	25.30	42.27
PD345-2	pyrite	18.7185	15.7161	38.9066	9.66	37.83	3.79	75.48	63.18	85.34	25.29	42.19
PD5-2-2	sphalerite	18.6413	15.7107	38.9458	9.66	38.36	3.84	78.05	61.23	84.66	25.14	45.39
PD5-11	sphalerite	18.7625	15.7209	39.0179	9.67	38.08	3.81	77.38	62.95	85.89	25.50	44.03
PD5-12-2	sphalerite	18.6028	15.7093	38.8990	9.66	38.37	3.84	77.86	61.11	84.45	25.16	45.28
PD5-13-2	sphalerite	18.7078	15.7174	39.0138	9.66	38.33	3.84	78.44	61.93	85.42	25.41	45.46
PD5-15	sphalerite	18.4055	15.6833	38.6487	9.63	38.20	3.84	74.87	59.05	81.56	23.97	43.37
PD5-16	sphalerite	18.5544	15.6859	38.8167	9.62	38.08	3.83	75.08	59.41	82.10	23.66	43.33
PD5-17	sphalerite	18.5295	15.6745	38.6232	9.60	37.32	3.76	70.07	60.28	80.97	22.93	38.31

6. Discussion

6.1. Metallogenic Epoch

The $^{207}\text{Pb}/^{206}\text{Pb}$ – $^{238}\text{U}/^{206}\text{Pb}$ concordant ages of the two cassiterite samples from the I ore body of the Bawang deposit are 93.1 ± 4.8 Ma and 85.3 ± 6.3 Ma, while the $^{207}\text{Pb}/^{206}\text{Pb}$ – $^{238}\text{U}/^{206}\text{Pb}$ isochron ages are 89.3 ± 6.3 Ma and 82.9 ± 5.3 Ma, indicating that the cassiterite is the product of mineralization in the early Late Cretaceous.

There are few studies on metallogenetic chronology in the Wuxu ore field; however, the only report which is accessible is that of Wei [47]. He obtained metallogenetic ages of 92 ± 11 Ma ($n = 18$, MSWD = 3.6) for the Bawang deposit and 103 ± 9.3 Ma ($n = 15$, MSWD = 1.4) for the Jianzhupo deposit by LA-ICP-MS U-Pb dating of cassiterite. The metallogenetic ages are consistent with those obtained in this paper within the error range, indicating that the tin-polymetallic mineralization in Wuxu ore field occurred in the Late Cretaceous. Previous studies on the chronology of the Nandan-Hechi metallogenic belt mainly focused on Dachang ore field (Figure 7): Wang et al. [27] obtained the $^{40}\text{Ar}/^{39}\text{Ar}$ plateau age of quartz in the Changpo-Tongkeng deposit of 94.52 ± 0.33 Ma, the $^{40}\text{Ar}/^{39}\text{Ar}$ isochron age of laser in situ of 91.4 ± 2.9 Ma, and the $^{40}\text{Ar}/^{39}\text{Ar}$ plateau age of quartz in the Longtoushan deposit of 94.56 ± 0.45 Ma. Cai et al. [20,48] obtained Rb-Sr isochron ages of 94.1 ± 2.7 Ma for the Kangma deposit and 93.4 ± 7.9 Ma for the Changpo-Tongkeng deposit. Li et al. [49] obtained a Rb-Sr isochron age of quartz in the Lamo deposit of 98.16 ± 5.8 Ma. Wang et al. [50] obtained a U-Pb isochron age of cassiterite of 95.8 ± 2.6 Ma. Guo J et al. [28] reported that the U-Pb age of cassiterite in multiple deposits of Dachang Ore field ranged from 90.3 ± 1.8 to 95.4 ± 4.9 Ma. Huang et al. [51] obtained a U-Pb date of cassiterite at 92.5 ± 4.4 Ma for the Longtoushan deposit. The results show that the tin-polymetallic mineralization time of Wuxu ore field is nearly the same as that of Dachang ore field, and they are the product of the same mineralization event in the early Late Cretaceous.

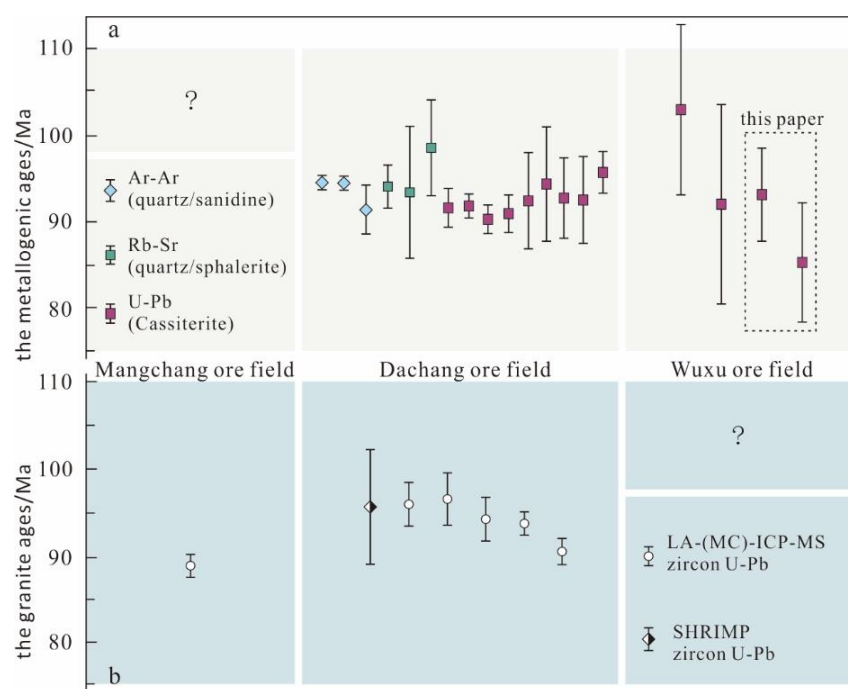


Figure 7. Metallogenetic ages of the main tin-polymetallic deposits (a) and the ages of related granite (b) in the Nandan-Hechi metallogenic belt [20,27,28,47–53]. ?—there is no data.

The tin-polymetallic metallogenetic ages are consistent with the high-precision zircon U-Pb ages (89–97 Ma) of granitic magmatic rocks of the Nandan-Hechi metallogenic belt reported in recent years, and there is a large time interval between this and the sedimentary age of ore-bearing surrounding rocks (Upper Carboniferous–Lower Permian). The coincidence of mineralization and diagenetic time provides strong support for the time relationship between tin-polymetallic mineralization and Late Yanshanian granitic intrusion in the Nandan-Hechi metallogenic belt. The spatial relationship shows that the mineralization presents three zones, including zinc–tin, antimony, and mercury–arsenic, from the (concealed) granite to the periphery, indicating the characteristics of magmatic–hydrothermal deposits. In conclusion, the tin-polymetallic mineralization in the Nandan-Hechi metallogenic belt should be attributed to Late Cretaceous granitic post-magmatic

hydrothermal processes rather than Late Paleozoic sedimentary exhalative processes. The boundary between the ore body and surrounding rock is distinct (the boundary is fissures of different sizes) [27], and the shear ore-controlled faults (such as F₅ of the Bawang deposit) further confirm that they are epigenetic deposits.

6.2. Ore-Forming Fluid Source

Carbon and oxygen isotopic composition of hydrothermal calcite provides an effective means of tracing the source of ore-forming fluids [7–11,54–57]. There are four sources of carbon in ore-forming fluids: (1) marine carbonate, for which the $\delta^{13}\text{C}_{\text{PDB}}$ values are mostly stable at 0‰; (2) metamorphic carbonate, with $\delta^{13}\text{C}_{\text{PDB}}$ values ranging from –12.5‰ to –4.7‰ [58]; (3) magma–mantle source, with $\delta^{13}\text{C}_{\text{PDB}}$ values of –5‰ to –2‰ and –9‰ to –3‰, respectively [59]; and (4) organic carbon in various rocks, for which the $\delta^{13}\text{C}_{\text{PDB}}$ values are about –25‰ [60]. When there is no graphite intergrowth with calcite in metallogenetic hydrothermal veins, the carbon isotopic composition of calcite can be approximated as the total carbon isotopic composition of ore-forming hydrothermal fluids [61]. As there is no graphite related to mineralization in the Bawang deposit, the carbon isotopic composition of the calcite in the ore body can approximately represent the carbon isotopic composition of the ore-forming hydrothermal solution.

The $\delta^{13}\text{C}_{\text{PDB}}$ values of calcite in the Bawang deposit were confined within a narrow range (–0.41‰ to 0.44‰) during mineralization. This range is between those of mantle-derived carbon (or magmatic carbon) (–3‰ to –9‰) [59] and marine carbonate (–2‰ to +2‰) [62]. Therefore, the carbon in the ore-forming fluid could not come from organic carbon sources, but it could come from granite (deep-source carbon) and marine carbonate. The $\delta^{18}\text{O}_{\text{SMOW}}$ value is concentrated within 13.85‰ to 15.40‰, close to the range of igneous rock (5‰~15‰) [58]. Similarly, Shao [63] obtained $\delta^{13}\text{C}_{\text{PDB}}$ values of calcite in the Tongkeng deposit ranging from –8.9‰ to –0.4‰, suggesting that the tin, zinc, and copper mineralization is involved with magmatic fluid and surrounding rock.

According to the $\delta^{13}\text{C}$ – $\delta^{18}\text{O}$ diagram [64] (Figure 8a), the calcite in the Bawang deposit falls between granite and marine carbonate and is far away from the sedimentary organic range, indicating that the fluid source is characterized by the mixing of magma and stratum. Meanwhile, $\delta^{13}\text{C}$ and $\delta^{18}\text{O}$ are negatively correlated (Figure 8b), similar to results for the metallogenetic calcite of Huize lead–zinc deposit in Yunnan province [65], the late-metallogenetic calcite of Jiaodong gold deposit [66], and the early metallogenetic calcite of Xianghualing polymetallic deposit in Hunan Province [67]. This negative correlation may be related to CO₂ degassing [68]. CO₂ degassing can increase the pH value of the fluid, leading to reduced solubility of tin in the solution, and it is conducive to cassiterite precipitation and mineralization [69]. CO₂ degassing can better explain the characteristics of weak wallrock alteration in the Bawang deposit.

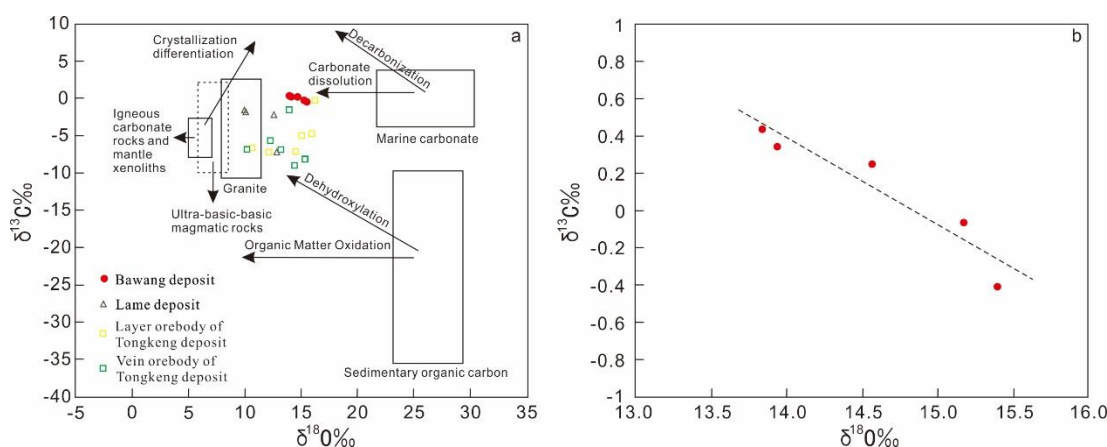


Figure 8. The $\delta^{13}\text{C}$ - $\delta^{18}\text{O}$ diagram of calcites from the main deposit in the Nandan-Hechi metallogenic belt (a) (modified after Liu et al. [64], the data from Liu [70], Tan et al. [71], and Ding et al. [72]) and the negatively correlated of $\delta^{13}\text{C}$ and $\delta^{18}\text{O}$ (b).

6.3. Source of Ore-Forming Material

Sulfur isotope detection is a mature method used to trace the source of ore-forming materials, and it is widely used to judge the genesis and sulfur source of ore deposits. In general, when using sulfur isotopes to study provenance, it is important to study the isotopic composition of the total sulfur in ore-forming hydrothermal fluids. Only when the sulfide composition is simple, and sulfosalt minerals are not present, can the isotopic composition of total sulfur in ore-forming hydrothermal fluids be substituted with sulfide $\delta^{34}\text{S}$ values [61,73]. There is no sulfosalt mineral in the Bawang deposit, so, it is feasible to use the $\delta^{34}\text{S}$ value of sulfide to replace the isotopic composition of total sulfur in the ore-forming hydrothermal fluid to study the provenance.

The sulfur isotope variation range of pyrite and sphalerite is narrow and the $\delta^{34}\text{S}$ values are similar ($-4.45\text{\textperthousand}$ to $-2.20\text{\textperthousand}$) (Figure 9), indicating they have the same sulfur source. According to previous studies, the sulfur isotopic composition of the main deposits in Dachang ore field ranges from $-8\text{\textperthousand}$ to 5\textperthousand [24,30,31,39,74–77], and that in Wuxu ore field ranges from $-5.2\text{\textperthousand}$ to $7.4\text{\textperthousand}$ [47]. The $\delta^{34}\text{S}$ value of pyrite in the strata varies from $-37\text{\textperthousand}$ to $-4\text{\textperthousand}$ [78], and the $\delta^{34}\text{S}$ value of Longxianggai granite varies from $-1.3\text{\textperthousand}$ to $-1\text{\textperthousand}$ [79]. However, Cheng [80] obtained $\delta^{34}\text{S}$ values ranging from $+4.46\text{\textperthousand}$ to $+16.36\text{\textperthousand}$. The $\delta^{34}\text{S}$ value by Cheng is close to that of granite in Figure 9. In the whole Nandan-Hechi metallogenic belt, the $\delta^{34}\text{S}$ value is higher when near the (concealed) granite, indicating that the sulfur is mainly derived from the magma. In the process of ore formation, hydrothermal fluid migrates from the center of granite to the periphery, and material favorable for mineralization extracted from the strata joins continuously.

Due to the large molecular mass of lead and the small relative mass difference between different lead isotope molecules, the isotopic composition of ore-forming elements usually does not change during leaching, transportation, and precipitation. Therefore, the characteristics and relations of the lead isotopic composition can be used to obtain information on the mineral source of the deposit.

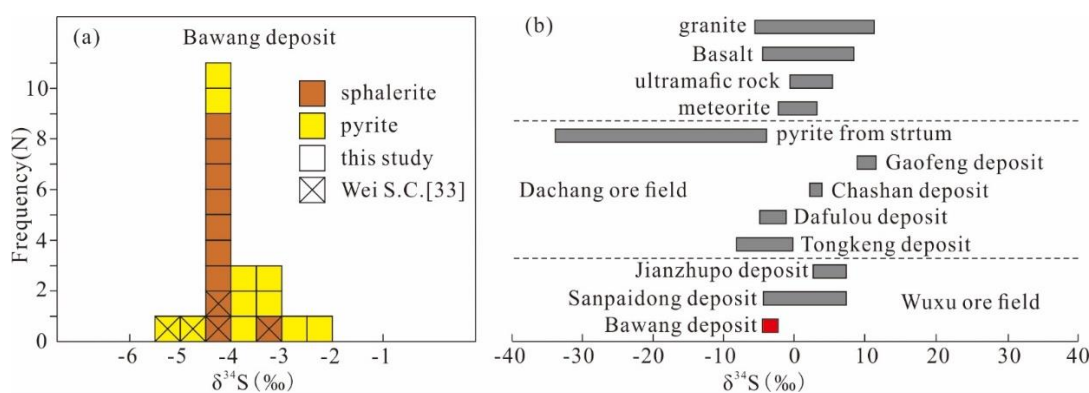


Figure 9. Histogram of sulfur isotopes of sulfides from the Bawang deposit (a); sulfur isotopic signatures of different deposits in the Nandan-Hechi metallogenic belt igneous rocks (b) [24,30,31,39,74–77].

The lead isotopic composition of the Bawang deposit is very stable and the distribution range is small, indicating that the metallogenic material may come from a single source or be dominated by a certain source. It is generally believed that the eigenvalues of the lead isotope source region, especially the μ value, can provide information on the geological process and reflect the source of lead. Lead with high μ values (greater than 9.58) is generally considered to be derived from upper crustal material, with enriched U and Th [60]. The μ values of the Bawang deposit are 9.60–9.67, with an average of 9.66 (greater than 9.58), indicating that the material came from the upper crust.

In the $^{207}\text{Pb}/^{204}\text{Pb}$ - $^{206}\text{Pb}/^{204}\text{Pb}$ and $^{208}\text{Pb}/^{204}\text{Pb}$ - $^{206}\text{Pb}/^{204}\text{Pb}$ tectonic environment evolution diagrams, all samples fall near the evolution line of the upper crust (Figure 10a) or between the orogenic belt and the lower crust (Figure 10b). In the lead isotope $\Delta\gamma-\Delta\beta$ genetic classification diagram (Figure 11), the samples are located in the upper crust and in the subduction zone (magmatism) mixed with upper crust and mantle. This indicates that the lead source of the Bawang deposit is mainly related to magmatism and comes from the crust–mantle mixed-source area, which is consistent with the Lamo deposit and Tongkeng deposit in Dachang ore field. In addition, it is very close to that of the Longxianggai granite in the Dachang ore field [80].

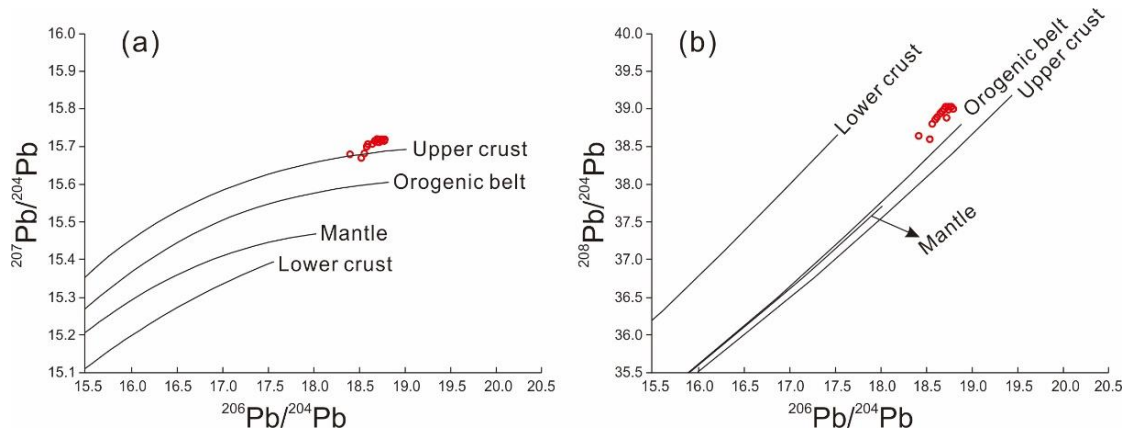


Figure 10. $^{207}\text{Pb}/^{204}\text{Pb}$ - $^{206}\text{Pb}/^{204}\text{Pb}$ uranogenic (a) and $^{208}\text{Pb}/^{204}\text{Pb}$ - $^{206}\text{Pb}/^{204}\text{Pb}$ thorogenic (b) for the Bawang deposit.

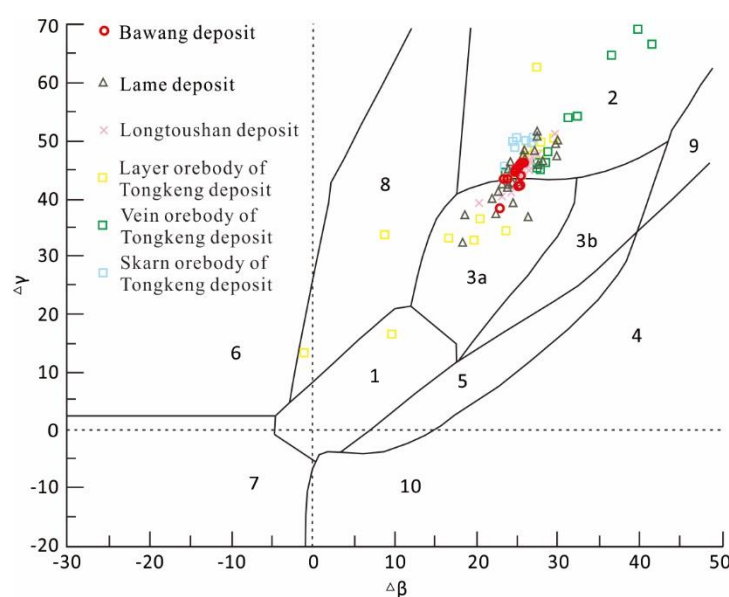


Figure 11. Genetic classification of Pb isotope $\Delta\gamma - \Delta\beta$ (base map according to Zhu et al. [81], the data of other deposit come from [17,21,24,30,53,72,82–85]).

7. Conclusions

- (1) The $^{207}\text{Pb}/^{206}\text{Pb}$ - $^{238}\text{U}/^{206}\text{Pb}$ concordant ages of samples BW4 and BW5 from the I ore body of the Bawang tin-zinc polymetallic deposit are 93.1 ± 4.8 and 85.3 ± 6.3 Ma, respectively, while the $^{206}\text{Pb}/^{207}\text{Pb}$ - $^{238}\text{U}/^{207}\text{Pb}$ isochron ages are 89.3 ± 6.3 and 82.9 ± 5.3 Ma, respectively. The cassiterite isochron ages of the two samples are consistent with concordant ages within the error range, indicating that the mineralization occurred in the early Late Cretaceous.
- (2) The C, O, and S isotopic compositions indicate that the ore-forming fluid of the Bawang deposit originated from the mixing of magmatic hydrothermal fluid and stratum. The Pb isotopic composition is consistent with that of the granite of the same age, indicating that ore-forming metals were mainly derived from magmatic hydrothermal solution.
- (3) From the comprehensive ore deposit geological characteristics and the isotope analysis, the Bawang deposit is a hydrothermal vein-type deposit, located in the external contact zone of Late Cretaceous granite, controlled by tectonic fractures, and formed by the interaction of magmatic hydrothermal fluid and carbonate rock. It is expected that large skarn-type ore bodies are present in the deep zone.

Author Contributions: Conceptualization, E.L. and D.H.; methodology, E.L.; software, G.Z. (Guangqian Zeng); formal analysis, D.H.; investigation, E.L., G.Z. (Guangqian Zeng), G.L., G.Z. (Guangjun Zou), P.L. and D.C.; data curation, P.L.; writing—original draft preparation, E.L. and D.H.; writing—review and editing, E.L. and G.Z. (Guangjun Zou); visualization, G.L. All authors have read and agreed to the published version of the manuscript.

Funding: This research was funded by Natural Science Youth Fund Project of Hunan Province (2019JJ50292) and National Key Research Development Plan (2017YFC0602602, 2016YFC0600207).

Conflicts of Interest: The funders had no role in the design of the study; in the collection, analyses, or interpretation of data; in the writing of the manuscript, or in the decision to publish the results.

References

- Peng, H.W.; Fan, H.R.; Zhang, R.Q.; Lan, T.G. Geochronological framework and ore genesis of the Tiantangshan Rb-Sn-W deposit, northeastern Guangdong, south China: Constraints from cassiterite and monazite U-Pb dating. *Ore Geol. Rev.* **2021**, *139*, 104457. [[CrossRef](#)]
- Li, C.Y.; Zhang, R.Q.; Ding, X.; Ling, M.X.; Fan, W.M.; Sun, W.D. Dating cassiterite using laser ablation ICP-MS. *Ore Geol. Rev.* **2016**, *72*, 313–322. [[CrossRef](#)]
- Zhang, R.Q.; Lehmann, B.; Seltmann, R.; Sun, W.D.; Li, C.Y. Cassiterite U-Pb geochronology constrains magmatic-hydrothermal evolution in complex evolved granite systems: The classic Erzgebirge tin province (Saxony and Bohemia). *Geology* **2017**, *45*, 1095–1098. [[CrossRef](#)]
- Cheng, Y.B.; Spandler, C.; Kemp, A.; Mao, J.W.; Rusk, B.; Hu, Y.; Blake, K. Controls on cassiterite (SnO_2) crystallization: Evidence from cathodoluminescence, trace-element chemistry, and geochronology at the Gejiu Tin District. *Am. Mineral.* **2019**, *104*, 118–129. [[CrossRef](#)]
- Liu, P.; Mao, J.W.; Lehmann, B.; Peng, L.L.; Zhang, R.Q.; Wang, F.Y.; Lu, G.A.; Jiang, C.Y. Cassiterite U-Pb dating of the lower Cretaceous Yanbei tin porphyry district in the Mikengshan volcanic basin, SE China. *Ore Geol. Rev.* **2021**, *134*, 104151. [[CrossRef](#)]
- Leonid, A.N.; Christopher, S.H.-D.; Richard, J.M. In situ LA-ICPMS U-Pb dating of cassiterite without a known-age matrix-matched reference material: Examples from worldwide tin deposits spanning the Proterozoic to the Tertiary. *Chem. Geol.* **2018**, *483*, 410–425.
- Yu, H.; Tang, J.R.; Li, H.; Kang, H.Y. Metallogenesis of the Siding Pb-Zn deposit in Guangxi, South China: Rb-Sr dating and C-O-S-Pb isotopic constraints. *Ore Geol. Rev.* **2020**, *121*, 103499. [[CrossRef](#)]
- Wu, J.H.; Chen, Y.L.; Zheng, C.Y.; Li, H.; Yonezu, K.; Tang, Y.Y.; Zong, Q. Genesis of the Longkou-Tudui gold deposit, Jiaodong Peninsula, eastern China: Constraints from zircon U-Pb dating, fluid inclusion studies and C-H-O-S stable isotopes. *Ore Geol. Rev.* **2021**, *139*, 104449. [[CrossRef](#)]
- Zhao, D.; Han, R.S.; Wang, L.; Ren, T.; Wang, J.S.; Zhang, X.P.; Cui, J.H.; Ding, J.J. Genesis of the Lehong large zinc-lead deposit in northeastern Yunnan, China: Evidences from geological characteristics and C-H-O-S-Pb isotopic compositions. *Ore Geol. Rev.* **2021**, *135*, 104219. [[CrossRef](#)]
- Shi, K.T.; Wang, K.Y.; Wang, R.; Ma, X.L.; Sun, L.X.; Yang, H. Geological, fluid inclusion, and O-C-S-Pb-He-Ar isotopic constraints on the genesis of the Honghuagou lode gold deposit, northern North China Craton. *Geochemistry* **2021**, *81*, 125807. [[CrossRef](#)]
- Xu, R.; Chen, W.; Deng, M.G.; Li, W.C.; Chen, F.C.; Lai, C.K.; Sha, J.Z.; Jia, Z.; Liu, W. Geology and C-O-S-Pb isotopes of the Fangyangshan Cu-Pb-Zn deposit in the Baoshan block (SW China): Implications for metal source and ore genesis. *Ore Geol. Rev.* **2021**, *132*, 103992. [[CrossRef](#)]
- Xu, J. *The Orefield Structure of Danchi Area, Guangxi*; Science and Technology Press: Beijing, China, 1988; p. 3.
- Liang, T.; Wang, D.H.; Cai, M.H.; Fan, S.K.; Yu, Y.X.; Wei, K.L.; Huang, H.M.; Zheng, Y. Metallogenic characteristics and ore-forming regularity of metallic deposits along Nandan-Hechi metallogenic belt in Northwestern Guangxi. *Miner. Depos.* **2014**, *33*, 1171–1192. (In Chinese with English abstract)
- Cai, M.H.; Zhao, G.C.; Zheng, Y.; Wang, X.B.; Guo, T.F.; Liu, H. Ore-controlling structural styles of the Nandan-Hechi metallogenic belt in Northwestern Guangxi. *Geol. Explor.* **2021**, *48*, 68–75. (In Chinese with English abstract)
- Han, F.; Hutchinson, R.W. Evidence for exhalative origin of the Dachang tin-polymetallic sulfide deposits—their geological and geochemical characteristics. *Miner. Depos.* **1990**, *9*, 309–324. (In Chinese with English abstract)
- Han, F.; Shen, J.Z.; Hutchinson, R.W. Adularia—an important indicator mineral of syngenetic origin for stratiform mineralization at the Dachang tin-polymetallic deposit. *Miner. Depos.* **1993**, *12*, 330–337. (In Chinese with English abstract)
- Chen, Y.C.; Huang, M.Z.; Xu, J.; Hu, Y.Z.; Tang, S.H.; Meng, L.K. *Geology of Dachang Tin Deposit*; Geological Publishing House: Beijing, China, 1993; pp. 1–361.
- Fu, M.; Changkakoti, A.; Krouse, H.R.; Gray, J.; Kwak, T.A.P. An oxygen, hydrogen, sulfur, and carbon isotope study of carbonate-replacement (skarn) tin deposits of Dachang tin field, China. *Econ. Geol.* **1991**, *86*, 1683–1703. [[CrossRef](#)]
- Fu, M.; Kwak, T.; Mernagh, T.P. Fluid inclusion studies of zoning in the Dachang tin-polymetallic ore field, People's Republic of China. *Econ. Geol.* **1993**, *88*, 283–300. [[CrossRef](#)]
- Cai, M.H.; Mao, J.W.; Liang, T.; Huang, H.L. Study on fluid inclusion of Tongkeng-Changpo deposit in Dachang tin polymetallic ore field. *Miner. Depos.* **2005**, *24*, 228–241. (In Chinese with English abstract)
- Liang, T.; Wang, D.H.; Cai, M.H.; Chen, Z.Y.; Guo, C.L.; Huang, H.M. Geochemical Characteristics and Prospecting potential of The Dachang Tin Polymetallic Deposit, Guangxi province. *Acta Geol. Sin.* **2008**, *82*, 967–977. (In Chinese with English abstract)
- Tanelli, G.; Lattanzi, P. The cassiterite-polymetallic sulfide deposits of Dachang (Guangxi, People's Republic of China). *Miner. Depos.* **1985**, *20*, 102–106. [[CrossRef](#)]
- Jiang, S.Y.; Han, F.; Shen, J.Z.; Palmer, M.R. Chemical and Rb-Sr, Sm-Nd isotopic systematics of tourmaline from the Dachang Sn-polymetallic ore deposit, Guangxi Province, P.R. China. *Chem. Geol.* **1999**, *157*, 49–67. [[CrossRef](#)]
- Zhao, K.D.; Jiang, S.Y.; Ni, P.; Ling, H.F.; Jiang, Y.H. Sulfur, lead and helium isotopic compositions of sulfide minerals from the Dachang Sn-polymetallic ore district in South China: Implication for ore genesis. *Mineral. Petrol.* **2007**, *89*, 251–273. [[CrossRef](#)]
- Chen, Y.C.; Huang, M.Z.; Xu, J.; Ai, Y.D.; Li, X.M.; Tang, S.H.; Meng, L.K. Geological characteristics and metallogenic series of Dachang cassiterite-sulfide polymetallic ore belt. *Acta Geol. Sin.* **1985**, *3*, 228–240. (In Chinese with English abstract)

26. Zhang, Z.G.; Li, X.L. Study on mineralization and material composition of DC ore field in Guangxi. *Geochimica* **1981**, *1*, 74–86. (In Chinese with English abstract)
27. Wang, D.H.; Chen, Y.C.; Chen, W.; Sang, H.Q.; Li, H.Q.; Lu, Y.F.; Chen, K.L.; Lin, Z.M. Dating the Dachang giant tin-polymetallic deposit in Nandan, Guangxi. *Acta Geol. Sin.* **2004**, *78*, 132–138. (In Chinese with English abstract)
28. Guo, J.; Zhang, R.Q.; Sun, W.D.; Ling, M.X.; Hu, Y.B.; Wu, K.; Luo, M.; Zhang, L.C. Genesis of tin-dominant polymetallic deposits in the Dachang district, South China: Insights from cassiterite U-Pb ages and trace element compositions. *Ore Geol. Rev.* **2018**, *95*, 863–879. [[CrossRef](#)]
29. Cai, H.Y.; Yang, Y.; Zhang, G.L. Preliminary discussion on stratabound ore control in Dachang tin deposit. *Miner. Resour. Geol.* **1983**, *3*, 72–77. (In Chinese with English abstract)
30. Qin, D.X.; Hong, T.; Tian, Y.L. *Geology and Technical Economy of No. 92 Orebody in Dachang Tin Deposit, Guangxi*; Geological Publishing House: Beijing, China, 2002; pp. 31–132.
31. Fan, D.L.; Zhang, T.; Ye, J.; Pasava, J.; Kribek, B.; Dobes, P.; Varrin, I.; Zak, K. Geochemistry and origin of tin-polymetallic sulfide deposits hosted by the Devonian black shale series near Dachang, Guangxi, China. *Ore Geol. Rev.* **2004**, *24*, 103–120. [[CrossRef](#)]
32. Yan, Y.F.; Liu, C.M.; Qin, D.X.; Jiang, K. Geological characteristics and metallogenic significance of the Devonian intermediate-basic volcanic rocks in the Dachang deposit, Guangxi Zhuang Autonomous Region. *Chin. J. Geochem.* **2013**, *32*, 110–118. [[CrossRef](#)]
33. Tu, G.C. Some problems of Sn–Pb–Zn mineralization. *Miner. Resour. Geol.* **1984**, *1*, 4–14. (In Chinese with English abstract)
34. Chen, J. On geological characteristics and formation mechanism of stratabound tin deposit in South China. *Geol. Rev.* **1988**, *34*, 524–532. (In Chinese with English abstract)
35. Lattanzi, P.; Corazza, M.; Corsini, F.; Tanelli, G.C. Sulfide mineralogy in the polymetallic cassiterite deposits of Dachang, P.R. China. *Miner. Depos.* **1989**, *24*, 141–147. [[CrossRef](#)]
36. Wang, J.C.; Yu, H.; Jiang, N.; Tang, J.R.; Wei, A.W. Temporal and spatial relation between the metallotectonic series and metallogenic series in the Dachang orefield, Guangxi. *J. Guilin Univ. Technol.* **2016**, *36*, 633–643. (In Chinese with English abstract)
37. Hu, R.G.; Zhao, Y.L.; Cai, Y.F.; Feng, Z.H.; Liu, X.J.; Zhou, Z.H.; Sha, P.Z. Characteristics of Biotite in the Granite Porphyry and Its Significance for Petrogenesis and Mineralization of Dachang Sn-Polymetallic Ore Deposit, Guangxi. *Earth Sci.* **2020**, *45*, 1213–1226. (In Chinese with English abstract)
38. Zeng, Y.F.; Liu, W.J. *Sedimentary Tectonic Evolution of Youjiang Basin in South China*; Geological Publishing House: Beijing, China, 1993; pp. 1–102.
39. Wang, D.M. A Study on the Characteristic and Origin of the Antimony Deposit in Danchi Metallogenic Belt, Guangxi. Master's Thesis, Chang'an University, Xi'an, China, 2012; pp. 1–107.
40. Cai, J.M.; Xu, X.H.; Liu, W.Z. Metallogenic characteristics and material sources of polymetallic deposit in Wuxu ore field, Guangxi. *J. Mineral. Petrol.* **1995**, *15*, 63–68. (In Chinese with English abstract)
41. Tu, J.R.; Cui, Y.R.; Zhou, H.Y.; Li, H.M.; Hao, S.; Li, G.z. Review of U-Pb dating methods for cassiterite. *Geol. Surv. Res.* **2019**, *42*, 245–253. (In Chinese with English abstract)
42. Xu, B.; Jiang, S.Y.; Luo, L. LA-MC-ICP-MS U-Pb dating of cassiterite from the Jianfengpo Sn deposit in the Pengshan Sn-polymetallic ore field, Jiangxi Province and its geological significance. *Acta Petrol. Sin.* **2015**, *31*, 701–708. (In Chinese with English abstract)
43. Yuan, S.D.; Peng, J.T.; Hao, S.; Li, H.M.; Geng, J.Z.; Zhang, D.L. Insitu LA-MC-ICP-MS and ID-TIMS U-Pb geochronology of cassiterite in the giant Furong tin deposit, Hunan Province, South China: New constraints on the timing of tin-polymetallic mineralization. *Ore Geol. Rev.* **2011**, *43*, 235–242. [[CrossRef](#)]
44. Ludwig, K.R. On the treatment of concordant uranium-lead ages. *Geochim. Et Cosmochim. Acta* **1998**, *62*, 665–676. [[CrossRef](#)]
45. Ludwig, K.R. *Isoplot: A Geochronological Toolkit for Microsoft Excel*. Special Publication No. 5; Geochronology Center: Berkeley, CA, USA, 2012; p. 70.
46. Friedman, I.; O'Neil, J.R. Chapter KK, Compilation of Stable Isotope Fractionation Factors of Geochemical Interest. In *Data of Geochemistry*, 6th ed.; Professional Paper 440-KK, KK1–12; Fleischer, M., Ed.; U.S. Geological Survey Publications: Washington, DC, USA, 1949; p. 1997.
47. Wei, S.C. Study on the Geological Characteristics and Genesis of the Main Deposits in the Wuxu ore field, Guangxi. Master's Thesis, Guangxi University, Nanning, China, 2020; pp. 1–86.
48. Cai, M.H.; Liang, T.; Wei, K.L.; Huang, H.M.; Liu, G.Q. Rb-Sr dating of the No. 92 orebody of the Tongkeng-Changpo deposit in the Dachang tin-polymetallic ore field, Guangxi, and its significance. *Geol. Miner. Resour. South China* **2006**, *31*–36. (In Chinese with English abstract)
49. Li, H.Q.; Wang, D.H.; Mei, Y.P.; Liang, T.; Chen, Z.Y.; Guo, C.L.; Ying, L.J. Lithogenesis and mineralization chronology study on the Lamo zinc-copper polymetallic ore deposit in Dachang orefield, Guangxi. *Acta Geol. Sin.* **2008**, *82*, 912–920. (In Chinese with English abstract)
50. Wang, X.Y.; Huang, H.W.; Chen, N.S.; Huang, X.Q.; Wu, X.K.; Hao, S.; Li, H.M. In-situ La-MC-ICP-MS U-Pb geochronology of cassiterite from Changpo-Tongkeng tin-polymetallic deposits, Dachang orefield, Guangxi. *Geol. Rev.* **2015**, *61*, 892–900. (In Chinese with English abstract)
51. Huang, W.T.; Liang, H.Y.; Zhang, J.; Wu, J.; Chen, X.L.; Ren, L. Genesis of the Dachang Sn-polymetallic and Baoshan Cu ore deposits, and formation of a Cretaceous Sn-Cu ore belt from Southwest China to western Myanmar. *Ore Geol. Rev.* **2019**, *112*, 103030. [[CrossRef](#)]

52. Wu, J.; Yuan, H.W.; Gan, N.J.; Wei, S.C.; Liao, J.; Zhang, J.; Liang, H.Y. Source characteristics of magmatic rocks and zircon U-Pb age in the Mangchang ore field, Danchi metallogenic belt, Guangxi. *Acta Petrol. Sin.* **2020**, *36*, 1586–1596. (In Chinese with English abstract)
53. Liang, T.; Wang, D.H.; Hou, K.J.; Li, H.Q.; Huang, H.M.; Cai, M.H.; Wang, D.M. LA-MC-ICP-MS zircon U-Pb dating of Longxianggai pluton in Dachang of Guangxi and its geological significance. *Acta Petrol. Sin.* **2011**, *27*, 1624–1636. (In Chinese with English abstract)
54. Rddad, L. The genesis of the Jurassic-hosted Mississippi Valley-type Pb-Zn ore deposit, Tigrinine-Taabast district (Central High Atlas, Morocco): Insights from fluid inclusion and C-O-S-Pb isotope studies. *J. Afr. Earth Sci.* **2021**, *174*, 104071. [CrossRef]
55. Duan, X.X.; Zeng, Q.D.; Wang, Y.B.; Zhou, L.L.; Chen, B. Genesis of the Pb-Zn deposits of the Qingchengzi ore field, eastern Liaoning, China: Constraints from carbonate LA-ICPMS trace element analysis and C-O-S-Pb isotopes. *Ore Geol. Rev.* **2017**, *89*, 752–771. [CrossRef]
56. Rddad, L.; Bouhlel, S. The Bou Dahar Jurassic carbonate-hosted Pb-Zn-Ba deposits (Oriental High Atlas, Morocco): Fluid-inclusion and C-O-S-Pb isotope studies. *Ore Geol. Rev.* **2016**, *72*, 1072–1087. [CrossRef]
57. Zheng, Y.F.; Chen, J.F. *Stable Isotope Geochemistry*; Science Press: Beijing, China, 2000; pp. 1–316. (In Chinese with English abstract)
58. Chen, J.; Wang, H.N. *Geochemistry*; Science Press: Beijing, China, 2004; pp. 1–418. (In Chinese with English abstract)
59. Taylor, B.E. Magmatic volatiles: Isotopic variation of C, H, and S. *Rev. Mineral. Geochem.* **1986**, *16*, 185–225.
60. Zartman, R.E.; Doe, B.R. Plumbotectonics—The model. *Tectonophysics* **1981**, *75*, 135–162. [CrossRef]
61. Ohmoto, H. Systematics of sulfur and carbon isotopes in hydrothermal ore deposit. *Econ. Geol.* **1972**, *67*, 551–578. [CrossRef]
62. Hoefs, J. *Stable Isotope Geochemistry*, 6th ed.; Springer: Berlin/Heidelberg, Germany, 2009; ISBN 978-3-540-70703-5, (Print).
63. Shao, Z.Z. Study on the Characteristics of Ore-Forming Fluid and Genesis of Dachang Tongkeng Tin Polymetallic Deposit, Guangxi. Master’s Thesis, Guangxi University, Nanning, China, 2019; pp. 1–80.
64. Liu, J.M.; Liu, J.J.; Zheng, M.H.; Gu, X.X. Stable isotope compositions of micro-disseminated gold and genetic discussion. *Geochimica* **1998**, *27*, 585–591.
65. Huang, Z.L.; Li, W.B.; Chen, J.; Han, R.S.; Liu, C.Q.; Xu, C.; Guan, T. Carbon and oxygen isotope constraints on mantle fluid involvement in the mineralization of the Huize super-large Pb-Zn deposits, Yunnan Province, China. *J. Geochem. Explor.* **2003**, *78–79*, 637–642. [CrossRef]
66. Mao, J.W.; Wang, Y.T.; Li, H.M.; Pirajno, F.; Zhang, C.Q.; Wang, R.T. The relationship of mantle-derived fluids to gold metallogenesis in the Jiaodong Peninsula: Evidence from D-O-C-S isotope systematics. *Ore Geol. Rev.* **2008**, *33*, 361–381. [CrossRef]
67. Yuan, S.D.; Peng, J.T.; Li, X.Q.; Peng, Q.L.; Fu, Y.Z.; Shen, N.P.; Zhang, D.L. Carbon, Oxygen and Strontium Isotope Geochemistry of Calcites from the Xianghualing Tin-Polymetallic Deposit, Hunan Province. *Acta Geol. Sin.* **2008**, *82*, 1522–1530. (In Chinese with English abstract)
68. Demny, A.; Harangi, S.Z. Stable isotope studies on carbonate formations in alkaline basalt and lamprophyre series: Evolution of magmatic fluids and magma-sediment interactions. *Lithos* **1996**, *37*, 335–349. [CrossRef]
69. Shuang, Y.; Bi, X.W.; Hu, R.Z.; Peng, J.T.; Su, W.C.; Zhao, C.S. Study on the ore-forming fluid geochemistry of the Furong tin polymetallic deposit, Hunan province, China. *Acta Petrol. Sin.* **2009**, *25*, 2588–2600. (In Chinese with English abstract)
70. Liu, J.X. Guangxi Calcite Tin Polymetallic Deposit Calcite Earth Chemical Characteristics Study. Master’s Thesis, Guangxi University, Nanning, China, 2019; pp. 1–57.
71. Tan, Z.M.; Tang, L.F.; Huang, D.J.; Cai, M.H.; Peng, Z.A.; Chang, J.; Zhao, J. Study on isotopes of carbon, hydrogen and oxygen and sources of ore-forming fluids in the Dachang tin orefield, Guangxi. *Miner. Explor.* **2014**, *5*, 738–743. (In Chinese with English abstract)
72. Ding, T.P.; Peng, Z.C.; Li, H. *Stable Isotope Study of Several Typical Deposits in Nanling Area*; Beijing Science and Technology Press: Beijing, China, 1988; pp. 21–44.
73. Ohmoto, H.; Rye, R.O. Isotopes of Sulfur and Carbon. In *Geochemistry of Hydrothermal Ore Deposits*; Barnes, H.L., Ed.; John Wiley & Sons: Hoboken, NJ, USA, 1979; pp. 509–556.
74. Li, Y. Genesis of the Lame Zn-Cu Deposit, Nandan. Master’s Thesis, China University of Geosciences, Beijing, China, 2017; pp. 1–73.
75. Cai, M.H.; Mao, J.W.; Liang, T.; Pirajno, F.; Huang, H.L. The origin of the Tongkeng-Changpo tin deposit, Dachang metal district, Guangxi, China: Clues from fluid inclusions and He isotope systematic. *Min. Depos.* **2007**, *42*, 613–626.
76. Liang, T. Study on the Metallogenic Mechanism of Changpo-Tongkeng Tin-polymetallic Deposit, Dachang. Ph.D. Thesis, Chang'an University, Xi'an, China, 2008; pp. 1–249.
77. Cheng, Y.S. Geological features and S isotope composition of tin deposit in Dachang ore district in Guangxi. *Trans. Nonferrous Met. Soc. China* **2014**, *24*, 2938–2945. [CrossRef]
78. Ye, X.S.; Yan, Y.X. Discussion on metallogenic geochemistry of surrounding rock medium in Dachang cassiterite-sulfide ore field. *Geochemical* **1987**, *2*, 123–131. (In Chinese with English abstract)
79. He, H.Z.; Ye, X.S. Study on source of ore-forming materials in Dachang ore field, Guangxi. *Guangxi Geol.* **1996**, *9*, 33–41. (In Chinese with English abstract)
80. Cheng, Y.S. Sulfur and Lead isotope geochemistry of Dachang intrusive plutons in Guangxi. *Acta Geol. Sin.* **2015**, *89*, 313–314.
81. Zhu, B.Q.; Li, X.H.; Dai, T.M. *Theory and Application of Isotope System in Earth Sciences—On the Evolution of Crust-Mantle in China*; Science Press: Beijing, China, 1998; pp. 224–226.

82. Wang, H.B. Study on metallogenic regularity and prospecting prediction of zinc and copper deposit, Lame, Dachang, Guangxi. Master's Thesis, Kunming University of Science and Technology, Yunnan, China, 2013; pp. 1–95.
83. Lei, L.Q. *The Minerogenetic Mechanism in the Dachang Superlarge Tin-Polymetallic Ore Deposit, Guangxi*; Guangxi Normal University Press: Guilin, China, 1998; pp. 1–68.
84. Han, F.; Zhao, R.S.; Shen, J.Z.; Rechard, W. Hutchinson. In *Geology and Origin of Ores in the Dachang Tin-Polymetallic Ore Field*; Geological Publishing House: Beijing, China, 1997; pp. 1–213.
85. Gao, J.Y. Pb isotopic evolution and its significance in ore genesis in the Dachang tin-polymetallic ore deposits. *Geol.-Geochem.* **1999**, *27*, 38–43. (In Chinese with English abstract)